



Synchrotron X-ray imaging study on the mechanism of solids transfer to bitumen froth during oil sands flotation 1: True flotation

Hanyu Zhang ^a , Liuyin Xia ^{a,*} , Ning Zhu ^b, Sergey Gasilov ^b, Iris He ^a, Xiaofan Ding ^b

^a Department of Chemical and Materials Engineering, University of Alberta, Edmonton, AB, Canada, T6G 2R3

^b Canadian Light Source Inc., 44 Innovation Blvd, Saskatoon, SK, Canada, S7N 2V3

ARTICLE INFO

Keywords:

Bitumen froth
Solids
Synchrotron radiation
X-ray micro-computed tomography (micro-CT)
True flotation

ABSTRACT

Unwanted mineral solids in bitumen froth can lead to increased solvent usage and higher hydrocarbon loss in downstream processing, negatively impacting the cost-effectiveness and sustainability of synthetic crude oil production. Enhancing the quality of bitumen froth with fewer solids is a goal for oil sands processors. This study presents an in-situ analysis of the particle size distribution and association of solids in bitumen froth, thereby uncovering solids transport mechanisms, such as true flotation. Oil sands flotation experiments were conducted with 30% pulp density, at 50 °C and pH 8.5. The collected bitumen froth was immediately characterized using synchrotron-based X-ray imaging by a monochromatic X-ray with photon energy of 60 keV provided by 05ID-2 beamline of the BioMedical Imaging and Therapy (BMIT) facility at the Canadian Light Source (CLS). This characterization method can finish a typical CT scan with 2000 projections in less than 3 min, and thus allows for in-situ imaging of freshly prepared bitumen froth without the need for special arrangements, such as freezing. 14,234 unwanted solids carried over into bitumen froth were visualized, 98.9 wt% of them were sand particles, which is consistent with mineral liberation analysis (MLA) results. This study introduced an innovative image segmentation technique to quantify the transfer of particles into the bitumen froth via true flotation. Statistical analysis revealed that approximately 53 wt% of sand particles were collected due to true flotation. Furthermore, the median particle size (P50) for sand particles entering froth by true flotation was determined to be 67.6 μm, significantly larger than the 30.6 μm observed for particles transferring through entrainment or entrapment.

1. Introduction

Oil sands, as the most abundant energy resource in Canada, have become essential for meeting global energy needs, due to their substantial contribution to the global crude oil supply (Khattak et al., 2018). In 2023, Canadian exports of crude oil reached a record high, totalling 230 million cubic metres (Record high crude oil production). The industrial (commercialized) bitumen concentration method for surface minded oil sands ore is water-based extraction process, in which froth flotation serves as the fundamental mechanism for separating bitumen from sand and other solid impurities (Masliyah et al., 2004). The resulting bitumen froth product typically contains 50–60 wt% bitumen, 30–40 wt% water, and 10–15 wt% solids (Rao and Liu, 2013; Khodaei et al., 2020). The solids content in a poor-quality bitumen froth would even higher. The unwanted mineral solids within bitumen froth directly result in increased solvent usage and higher hydrocarbon loss in downstream processing (Polischuk et al., 2023; Rana et al., 2019),

thereby negatively impacting both the cost-effectiveness and sustainability of synthetic crude oil production.

Given these implications, companies in the oil sands industry are actively pursuing methods to produce higher quality bitumen froth with fewer solids. However, there is a knowledge gap for uncovering reasons behind the presence of mineral solids in bitumen froth during froth flotation. It is widely assumed that solid particles report to the froth layer during flotation through a combination of complex mechanisms, including true flotation, mechanical entrainment, slime coating, and unliberated or coagulated bitumen-solid aggregates (Zhou et al., 2017a). The concepts of true flotation, mechanical entrainment, and slime coating are all adopted from mineral processing (Zhou et al., 2018). True flotation refers to the process where a particle collides with a rising bubble and adheres to its surface, ultimately reporting to the froth layer (George et al., 2004). Mechanical entrainment involves particles being carried from the pulp into the froth by the interstitial liquid (George et al., 2004; Wang et al., 2015). Slime coating occurs when fine

* Corresponding author.

E-mail address: liuyin@ualberta.ca (L. Xia).

unwanted solids form a layer on the target mineral, allowing it to enter the froth layer along with the coated particles (Yu et al., 2017). Of these mechanisms for solids transportation, true flotation is the only selective physical process. Minerals carried to the froth by mechanical entrainment and slime coating are non-selective. During flotation, to distinguish true flotation from mechanical entrainment, the researchers initially used two sets of flotation tests: one with only frother and the other using both frother and collector. Through comparison of mineral recoveries from two batch flotation tests, the solids carried over by true flotation can be identified (Trahar, 1981). Similar strategies were applied by using depressants. It was reported that adding a high dose of depressant ($>500 \text{ g/t}$) to inhibit true flotation can identify how much solids carried over through entrainment (Mhone et al., 2017). However, the addition of collector or depressants may impact the flotation dynamics, which changes the amount of both true flotation and entrainment particles, making these methods less accurate. Previously, a modified Hallimond tube with a narrow throat (Siwek et al., 1981) was used in froth flotation without any frother. It was assumed single-bubble passage eliminates entrainment, so particles collected were solely through true flotation (Wang and Liu, 2021a). Additionally, Warren (1985) proposed a method based on how much water being pulled out, summarized by the following equations:

$$R_M = F_M + e_M \times W_{\text{Water}} \quad (1)$$

$$R_G = e_G \times W_{\text{Water}} \quad (2)$$

where R_M and R_G represent the recovery amount of floatable (hydrophobic) mineral and non-floatable (hydrophilic) gangue. F_M is the true flotation component, e_M and e_G are entrainment factors for floatable mineral and non-floatable gangue, and W_{Water} denotes the weight of water recovered within a given time. According to Warren's model, when the amount of water pulled out during flotation is extrapolated to zero, the amount of recovered floatable minerals can be considered representative of true flotation amount. Zhou and coworkers (Zhou et al., 2017a) have applied this water recovery method to analyze particle transfer into the froth layer during oil sands flotation, distinguishing fine solids recovery by true flotation from that by entrainment. These methods are based on assumptions and require altering flotation conditions during operation, which limits their accuracy and real-time applicability.

The behavior of particles in fluid during froth flotation can be tracked and observed. The methods include particle tracking velocimetry (Dracos, 1996), laser doppler velocimetry (Tropea et al., 2007), particle image velocimetry (Raffel et al., 2018), and particle shadow velocimetry (Estevadeordal and Goss, 2005). However, these optical based methods are not suitable for observation of the froth layer due to the opacity arises from the irregular distribution of numerous bubbles, which refract light and hinder visibility (Lappan et al., 2023). Moreover, bitumen froth itself is dark and opaque, further omitting the applicability of optical methods. Transmission imaging methods can overcome the opacity issue. For example, Waters et al. (2008) used positron emission particle tracking (PEPT) to study the motion of a pyrite tracer in slurry and observed its attachment to bubbles within a Denver flotation cell. Heitkam et al. (2018) used transmission imaging with neutrons to observe gadolinium-based particles in froth system, and recorded the motion of particles in froth layer during froth rinsing. However, these methods also have limitations. The PEPT method can only track a very limited number of tracer particles in order to differentiate them. In Waters et al.'s work (Waters et al., 2008), only one pyrite particle labeled with ^{18}F was tracked. Transmission imaging with neutrons showed low contrast-to-noise ratio for smaller particles (Lappan et al., 2020). In Heitkam et al.'s work, the resolution was approximately $200 \mu\text{m}$, suggesting that transmission imaging is limited to capturing only coarse particles. (Heitkam et al., 2018).

The unwanted solids in bitumen flotation presents a particular

complexity, requiring new insights into the mechanisms of solids carryover. Existing studies have generally relied on off-site analysis methods, involving washing out bitumen from particle's surface by toluene using Dean Stark method, then analyzing the particle size distribution and mineralogy off-site (Li and Xu, 2020; Kotlyar et al., 1998; Zhao et al., 2016; Hooshiar et al., 2012). No published research has directly examined the distribution and association of mineral solids in bitumen froth in-situ. Spatial information for studying the mechanisms of mineral solids transport to froth is still lack, particularly regarding the aggregation of bitumen droplets, particles and air bubbles.

The aforementioned tracking methods enable in-situ studies of particles behavior in the system. However, beyond the limitations of these methods themselves as previously discussed, they are also incapable of distinguishing particle size and type. To overcome this limitation, X-ray micro-computed tomography (micro-CT) has emerged as a viable imaging tool, capable of penetrating froth layers to reveal bubble clusters and enabling mineral identification based on density contrasts (Solórzano et al., 2013; Mathews et al., 2017; Anzoom et al., 2024). In fact, micro-CT has been widely used for sample characterization across fields such as petrology, mineralogy, and geo-metallurgy for sample characterization as a non-destructive testing method. It has been proven instrumental in determining microstructure (Ghorbani et al., 2011), quantitative characterization of pore size distributions and morphology (Chen et al., 2018), and analysis of mineral grade and distribution and mineral association (Miller et al., 2009). Despite its advantages, however, traditional lab-based micro-CT imaging techniques require several hours to complete a full scan to ensure image quality and capture sample details. For example, Anzoom et al. (2024) conducted a scan involving 2880 projections, with a duration of 1.5 h to achieve the required image quality. In the dynamic environment of bitumen froth, where bubbles are in constant motion and susceptible to breakup and coalescence, it is practically impossible to maintain sample stability over such an extended CT scan duration. Anzoom et al. (2024) proposed a method to address this issue by freezing bubble clusters with a customized setup, ensuring that the agglomerates remained stationary during the CT scan. However, this freezing process altered both the shape and positioning of the bubbles, which in turn introduced certain limitations and inaccuracies into the observations.

In contrast, the state-of-the-art synchrotron radiation technique offers a superior alternative. Synchrotron radiation is electromagnetic radiation produced by low-mass charged particles, such as electron, moving at relativistic speeds (i.e., near the speed of light) as they experience radial acceleration due to deflection in a magnetic field. Fig. 1 (L'Annunziata, 2023) illustrates the principle of synchrotron radiation generation. As can be seen, electrons travel at nearly the speed of light in a storage ring, emitting synchrotron radiation when their trajectory is bent by a magnetic field, with the radiation concentrated into a cone at an angle on the order of γ^{-1} . γ refers to the relativistic factor of a particle, which approaches infinity as the particle's speed close to the speed of light. When the speed of particle is large enough, the radiation

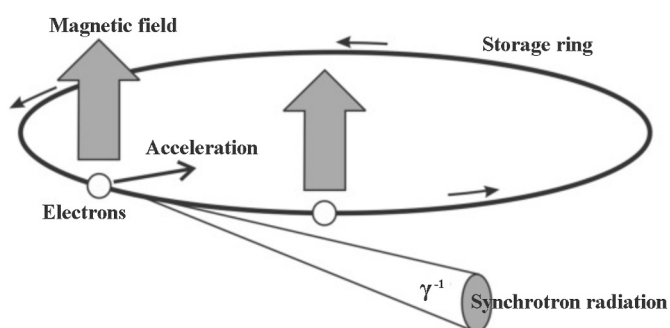


Fig. 1. Schematic diagram of synchrotron radiation generation principle, reproduced from reference (L'Annunziata, 2023) with permission from Elsevier.

will be concentrated within a narrow cone in the forward direction. Take the synchrotron at the Canadian Light Source (CLS) as an example, the electrons are energized to 2900 MeV, reaching 99.999998% of the speed of light in the booster ring, before entering the storage ring to generate synchrotron radiation (What is a synchrotron). At this speed, the value of γ^{-1} becomes extremely small, resulting in highly collimated radiation that significantly reduces beam divergence and achieves exceptionally high brightness. During operation, the booster ring transfers up to 600 electrons into the storage ring, achieving an average circulating current of 220 mA (What is a synchrotron). These high-density, high-frequency circulating electron beams further enhance the exceptional brightness of synchrotron radiation. In addition, to bend the electron trajectory in the storage ring, CLS employs large (6800 kg) magnets along with insertion devices such as wigglers and undulators. These devices force the electrons to oscillate, generating even more intense X-rays (What is a synchrotron). In generally, the radiation produced by synchrotron is about 10^6 as intense as that produced in conventional X-ray tubes (Adams et al., 1998). The extremely high brightness and intensity of synchrotron radiation enable the use of monochromators to produce high-quality monochromatic X-rays with enough brightness. These X-rays are particularly advantageous as they effectively eliminate beam-hardening artifacts caused by broadband spectra in CT imaging, enhancing contrast and improving quantitative analysis (Lifton and Malcolm, 2021). High-brightness and highly collimated monochromatic radiation provided by synchrotron enables micro-CT to capture images with spatial resolution at the micrometer scale and the temporal resolution at the microsecond scale (Rack et al., 2010).

Synchrotron-based X-ray imaging has been successfully applied to study pore structures, bubble formation, and foam drainage (García-Moreno et al., 2017; Kamm et al., 2017). It is anticipated that the imaging will be fast enough to capture the froth's internal microstructure before bubble breakup and coalescence occur, thus preserving the froth's natural state for accurate analysis. However, despite its immense potential, synchrotron X-ray imaging for real bitumen froth has never been reported in existing literature. In this work, we employed synchrotron X-ray micro-CT to image bitumen froth generated through flotation and analyzed its microstructure, with a focus on examining the distribution of sands and heavy mineral solids. Additionally, an image segmentation method was applied to determine whether the particles entered the froth layer through true flotation, as indicated by their association with air bubbles.

2. Methodology

2.1. Bitumen froth preparation

The oil sands ore sample used in this work was collected from a mine site situated in the Athabasca region of northern Alberta, Canada. A Denver D-12 flotation machine was used to conduct flotation to recover bitumen from the ore. The flotation parameters were set with 30% pulp density, at 1000 rpm, 3 L/min air flowrate, pH 8.5 and the bitumen froth flotation was conducted at 50 °C. The aerated froth was promptly collected at the beginning of flotation, and immediately transferred into a cylindrical container with a 10 mm diameter and a height of 4–5 mm. This immediate transfer and the use of a shallow container were essential to preserve the overall integrity and to maintain the fresh bitumen froth's original microstructure. The fresh samples were then subjected to synchrotron-based micro-CT scanning without delay. In addition to the froth samples prepared for CT scanning, other froth products collected from flotation were dried in an oven and subsequently treated using the Dean-Stark method to remove bitumen. The remaining solid fractions were isolated for further compositional analysis.

2.2. Assay of solid particles

Solid particles (5 g) from the flotation froth were combined with 15 mL of pre-mixed, two-component epoxy resin and poured into 30 mm diameter polypropylene molds, and allowed to cure overnight. After curing and demolding, the sample was polished using 1 μm diamond polishing compound to prepare the analytical surface. The polished sample was coated with a 15 nm thick layer of amorphous carbon to ensure electrical conductivity of the sample surface. Mineral liberation analysis (MLA) was conducted at an accelerating voltage of 25 kV and a beam current of 10 nA, with data collected in Particle Mineral Analysis (PMA) mode at a spacing of 5 μm. Modal mineralogy was calculated from the combined analysis of the backscattered electron (BSE) images and the mineral identification from the energy dispersive spectroscopy (EDS) data. The volumetric abundance of the minerals was converted to mass percent from density data for typical mineral compositions.

2.3. Image acquisition

High-resolution X-ray imaging of the fresh bitumen froth was conducted at the 05ID-2 beamline of the BioMedical Imaging and Therapy (BMIT) facility at the CLS. This beamline provided a monochromatic X-ray with photon energy of 60 keV. Experimental hutch of SOE-1 was used (Wysokinski et al.) for micro-CT images acquisition. A schematic diagram of image acquisition was shown in Fig. 2. In order to improve the contrast to better distinguish the components in bitumen froth, a phase-sensitive imaging method, propagation-based imaging (PBI, also called in-line phase contrast imaging), was applied. Propagation distance (i.e., the distance between the sample and the detector) is the crucial factor to determine the resulting image contrast in PBI (Bravin et al., 2012). In this study, after several trials to find the optimal position, the propagation distance was determined to be 0.6 m. The X-ray detector (AA60 beam monitor (Hamamatsu, Japan) with the sCMOS camera of PCO Edge 5.5) provided a pixel size of 6.5 μm. The exposure time per projection was 50 ms. A typical CT scan with 2000 projections captured in 180° took less than 3 min. This rapid and detailed imaging provided crucial volumetric data for analyzing the internal microstructure of the bitumen froth.

2.4. Image processing

An image processing toolkit developed based on the open source *ufo framework*, *tofu ez* (Faragó et al., 2022), was used to reconstruct images after the CT data acquisition. As shown in Fig. 3(a), the reconstructed images had ring artifacts that were semi-circular and ring-shaped artifacts on projection. It is caused by small errors in detector pixel values to persist throughout CT acquisition. The existence of ring artifact will impact subsequent segmentation. To remove ring artifacts in these images, we used a Matlab application developed by Wei and coworkers (Wei et al., 2013). The removal starts by transforming the images into

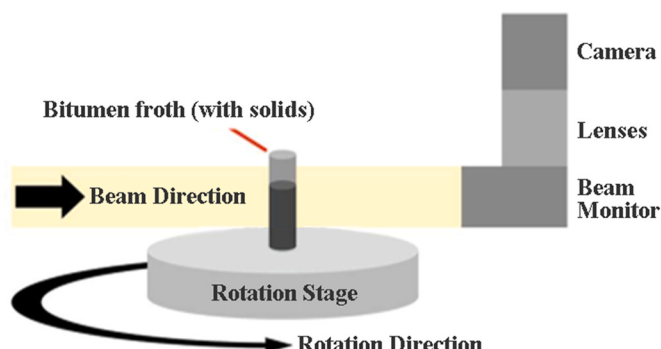


Fig. 2. Schematic diagram of X-ray micro-CT image acquisition process.

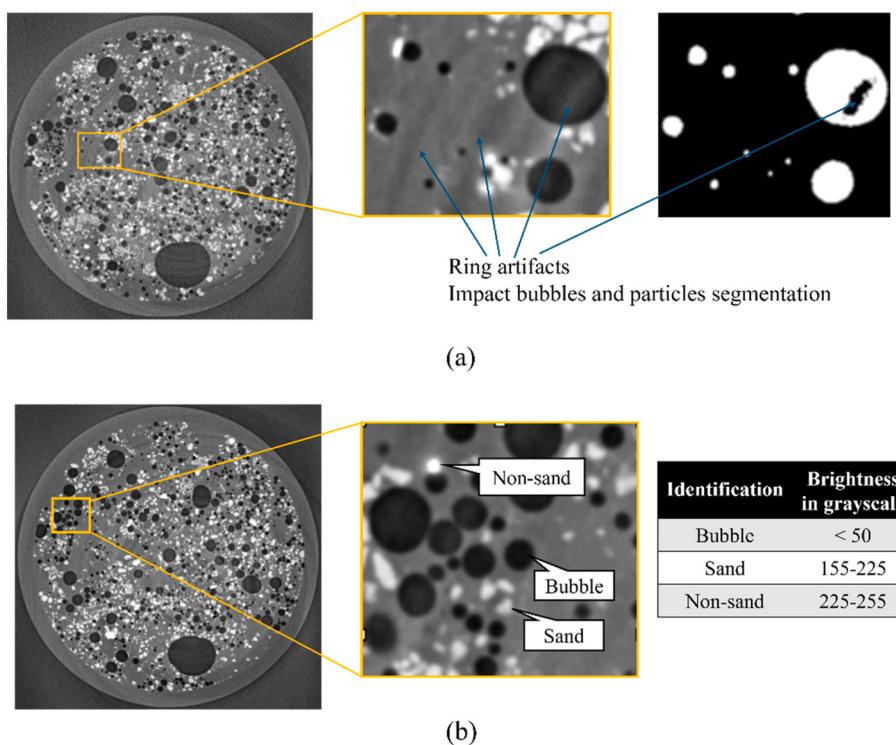


Fig. 3. Diagram of a reconstructed slice (a) before ring artifacts removal, and (b) after ring artifacts removal.

polar coordinates, and then the polar image is decomposed into four image components using a 2D wavelet transform: the low-pass band image component, and the components from horizontal, vertical, and diagonal details bands. A 2D Fourier transform is applied to the vertical details band image component only, as the ring artifacts become vertical lines in the polar coordinates. Gaussian filtering (Marr and Hildreth, 1980) is then applied in the Fourier domain along the abscissa direction to suppress the vertical lines. After above processing, inverse Fourier transform followed by inverse wavelet transform are performed to get the corrected polar image. The corrected polar image is then converted back to Cartesian coordinates to produce an image with reduced artifacts. Fig. 3(b) shows the reconstructed image after ring artifacts removal. In addition, the bright dots in the enlarged image in Fig. 3(b) indicates that the objects there have a higher density. In oil sands, these particles should be heavy minerals, such as rutile (TiO_2) and zircon (ZrO_2). We refer to these bright particles (with a grey level between 225 and 255) as non-sand minerals. The irregular areas with medium grey level (155–225) are the most common solid components in oil sand, such as quartz and clay, collectively referred to as sands. The circular areas with lower grey values represent air bubbles.

2.5. Image segmentation

ImageJ was used to segment particles and air bubbles from the reconstructed slices. During the image segmentation for bubbles, we used a dynamic enhancement algorithm (Kohler, 1981), which is incorporated in ImageJ. It allows us to set parameters of threshold of grey level enhancement, denoted as T . By choosing a value of T , the grey value of the original image will be converted the enhance data plot. According to the actual situation of the interference image, the distribution range of the grey value of the bubble area is narrow. The segmentation accuracy for air bubbles using this simple thresholding method is acceptable. The local images of a slice obtained at different step of the segmentation using thresholding method are shown in Fig. 4.

In this bitumen froth system, particles unlike the round and uniform shape air bubbles, have irregular shapes with sharp corners and edges,

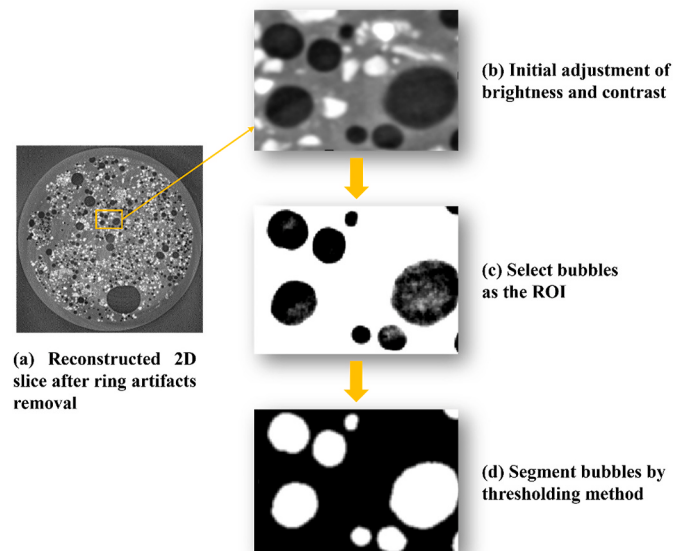


Fig. 4. Flow diagram for the thresholding segmentation of bubbles in a slice.

making it challenging for segmentation algorithms to accurately identify and delineate their boundaries. The thresholding techniques, even with grey level enhancement, are insufficient for accurate segmentation of mineral particles. To achieve more precise minerals segmentation, we employed the watershed method (Seal et al., 2015). It simulates the rise and flooding of water from local minima, dividing the image into regions. Thus, it can effectively separate overlapping particles by treating the image as a topographic surface, where high-intensity regions are peaks and low-intensity regions are valleys. In comparison to the thresholding method, watershed method helps in delineating individual particles even when they touch or slightly overlap. Fig. 5 illustrates the

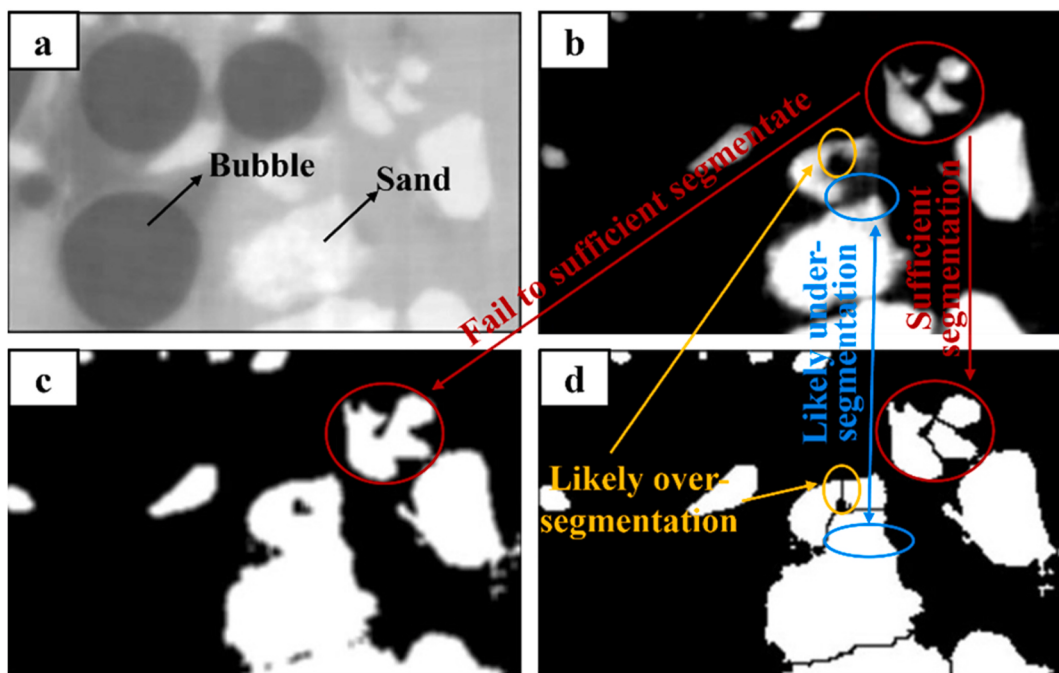


Fig. 5. Images of a local area for (a) reconstructed original image, (b) binary mask with particles selected, (c) particles segmented by thresholding method, and (d) particles segmented by watershed method.

obtained images by both thresholding and watershed techniques, where panel (a) shows the reconstructed original image, and (b) shows the selected particles as region of interest (ROI). Panel (c) and (d) shows the segmentation results using thresholding and watershed methods, respectively. The thresholding segmentation method often merges closely positioned particles into single clusters, as seen in the upper right corner of panel (b) and (c) in red circles. Conversely, the watershed method accurately distinguishes these particles (panel d). Although over segmentation may occur with the watershed method, as indicated by the yellow circles, it has minimal impact on our study because of the large sample size. We analyzed 100 reconstructed slices, each containing more than 1000 identified particles. A single digit number of over-segmented or under-segmented particles is negligible compared to the overall number of particles, ensuring the particle size distribution remains largely unaffected. Thus, we adopted the watershed method that provides a more robust and precise segmentation for mineral particles in the bitumen froth system.

In froth flotation, particles attached to air bubbles are considered to be brought directly to the froth layer through true flotation. The composition and content of these particles are important characterization in flotation (Ross, 1997). To precisely identify the particles attached to air bubbles, our work introduced an innovative approach to segment the overlay between particles and bubbles. The detailed image segmentation procedures are as follows (Fig. 6).

- 1) the reconstructed image (panel a) was segmented to isolate particles and bubbles using the previously mentioned methods, resulting in the regions of ROIs shown in panel (b).
- 2) Each segmented particle and bubble were then dilated by two pixels to generate the updated ROIs, as shown in panel (c). The ROIs were assigned a value of 1, and the background was set to 0.
- 3) The overlay area of the dilated bubbles and particles were segmented using the “AND” function of ImageJ, producing an “overlay” image shown in panel (d).
- 4) The overlay was further dilated by two pixels (panel e), and we then combine this dilated overlay with the original, non-dilated particles mask to obtain a combined mask (panel f).

- 5) The combined mask was then segmented using the thresholding method, the particles with air bubble attached or not attached are differentiated as shown in panel (g).

This method accurately mapped the particles attached to bubbles (i.e., those carried over to the froth layer due to true flotation attaching to air bubbles). Following segmentation, the area of each selected particle was extracted for further quantitative analysis.

The 3D model of the bitumen froth was created using Avizo software developed by Thermo Fisher Scientific. The stack of 100 slices binary masks was imported, and an ortho slice linked to the mask was then created for visualization. Fig. 7 shows the 3D diagram of air bubbles, mineral particles, and each individual entity. Each particle was labeled to obtain detailed information such as volume. The volumes of the 3D particles were calculated by voxel counting by Avizo software. To express their sizes, the equivalent spherical diameter was determined by calculating the diameter of a sphere with a volume equal to that of the particle. Based on the volume and equivalent diameter, characterization of the particle in the fresh bitumen froth was reported in the results and discussion section.

3. Results and discussion

3.1. Sand and non-sand minerals

The synchrotron-based micro-CT imaging method enables in-situ visualization of the particle distribution and positions within the fresh bitumen froth. The visualization of particles within the bitumen froth provided detailed insights into the particle size distribution, overcoming the limitations of traditional off-site analysis methods. As mentioned previously, 3D model was built using the 100 reconstructed slices; the characterization results of the particles (sand and non-sand) are presented in Fig. 8 (a). Due to the large differences between data within the same group, the vertical axes in the charts are represented using a logarithmic scale. As can be seen, 13, 616 sand particles in total were detected from the 3D image, whereas only 618 non-sand particles (heavy minerals) were counted. This indicate that sand particles constitute the majority, making up 95.66% of the total number of

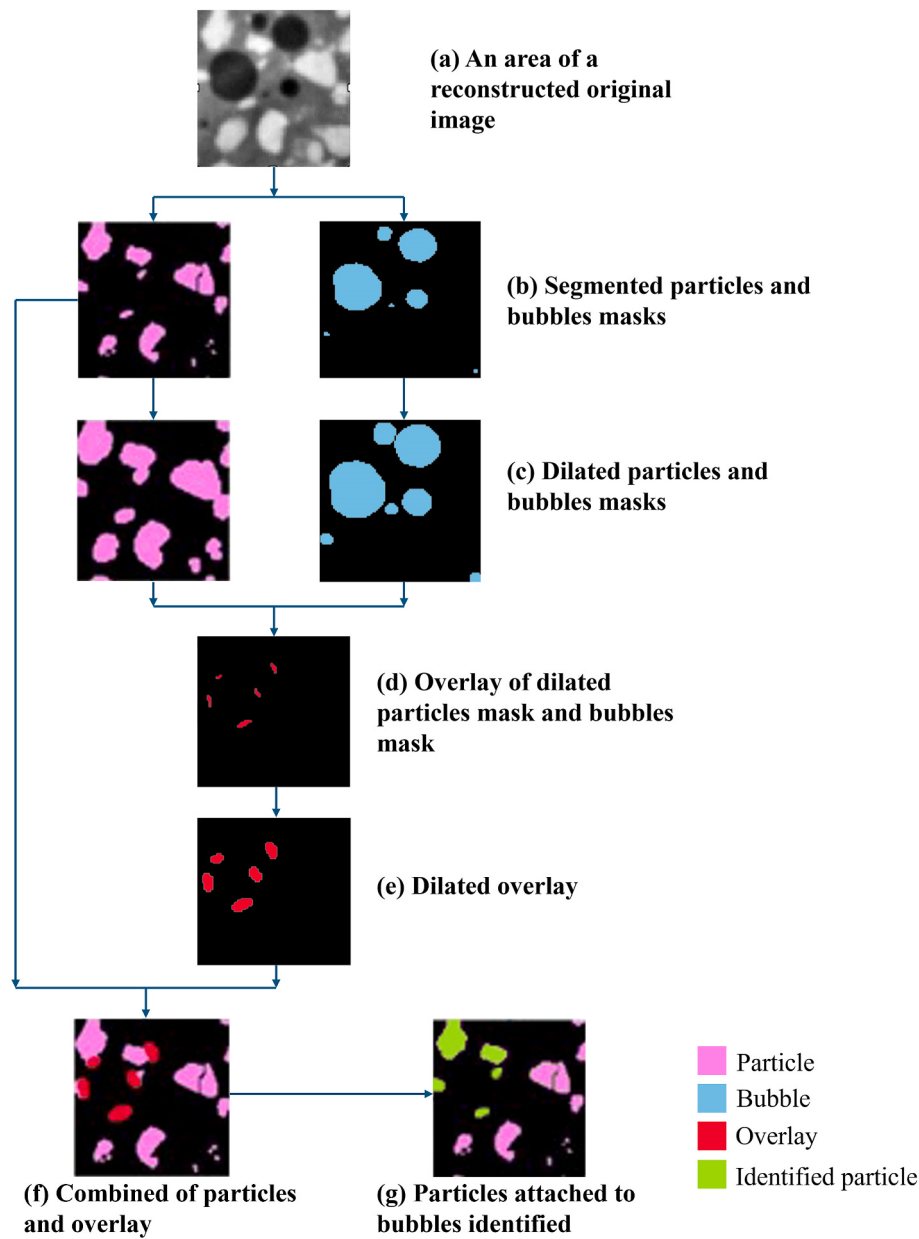


Fig. 6. Image processing procedure for identifying particles attached to bubbles. While the original images are in grayscale, colors have been applied here for easier distinction of the different components.

particles (both sand and non-sand particles). The total volume of sand particles is $5.898 \times 10^9 \mu\text{m}^3$; and the total volume of non-sand particles is significantly lower at $0.040 \times 10^9 \mu\text{m}^3$. According to the characterization of heavy minerals in Athabasca oil sands ore (Liu et al., 2006), the heavy minerals are primarily rutile (TiO_2) and zircon (ZrO_2), with average content of approximately 0.35 wt% for TiO_2 and 0.032 wt% for ZrO_2 (McCosh, 1996). Assuming a specific density of 2.68 g/cm^3 for sand particles and treating non-sand minerals as TiO_2 with a specific density of 4.23 g/cm^3 , the mass percentage calculated based on the volume of percentage was 98.9 wt% for sand and 1.1 wt% for non-sand minerals. This closely matches the referenced mineralogical analysis for Athabasca bitumen froth, in which the TiO_2 content is 1.36 wt% (Kaminsky, 2008). TiO_2 carrier minerals in the bitumen froth are typically small, with about 6–7 wt% being less than $2 \mu\text{m}$ (Kaminsky, 2008). Given that the resolution of our micro-CT images is $6.5 \mu\text{m}$ per pixel, some TiO_2 cannot be detected. This explains why the analyzed result (1.1 wt%) from the 3D image is slightly lower than the off-site analysis

result (1.36 wt%). An X-ray detector with higher resolution ($2 \mu\text{m}$) will be used in our next report in this series to achieve a more accurate result for more complex analysis. Fig. 8 (b) shows the particles characterization results obtained from 2D slices, where the particles amount was counted from all the 100 slices (these 100 slices include multiple counts of the same particle. This is why the number of particles observed here is an order of magnitude higher than the results obtained from the 3D image, which represents the true particle count) and the particles area was the average for per slices. In total, 146, 265 sand particles were detected in all the 100 slices. Both 2D and 3D imaging methods yielded a similar proportion of sand particles (approximately 97% sand), confirming the consistency of the two image processing techniques. The discrepancies from algorithms are negligible; therefore, only 2D images were processed and utilized in subsequent studies to quantify particles transferring into the froth through true flotation.

In addition, 3, 657 non-sand particles were segmented, accounted for about 2.45% of total number of all particles. The non-sand particles

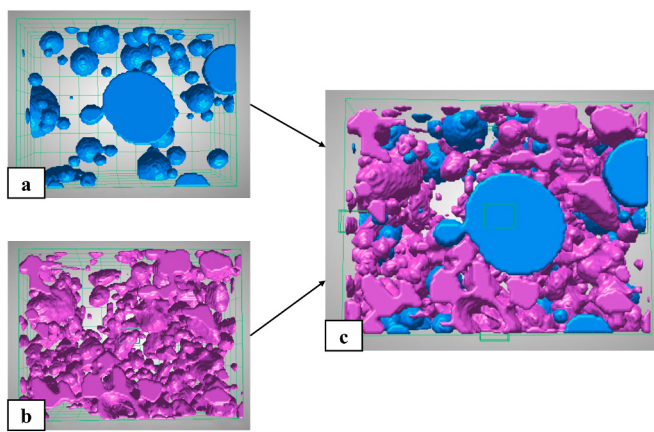


Fig. 7. Diagram of 3D view of (a) air bubbles, (b) particles, and (c) each individual entity.

covering an area of $62,330 \mu\text{m}^2$ per slice, making up about 1.67% of the area for all particles.

Fig. 9 presents the major mineral composition and corresponding concentrations within the solids in bitumen froth, as analyzed by MLA. The results indicate that quartz constitutes the predominant component, reaching 86.08 wt%, which is significantly higher than any other mineral present. Additionally, minor amounts of orthoclase (3.91 wt%) and kaolinite (2.08 wt%) were detected, along with very small amount of muscovite, pyrite, rutile, almandine, and zircon. The combined content of rutile and zircon amounts to 1.63 wt%. These results closely align with the concentrations of heavy minerals obtained through CT image analysis, further supporting the accuracy and feasibility of the image-based analytical approach.

Table 1 presents a detailed comparison of the particle size distribution for both sand and non-sand (i.e., heavy minerals) particles, analyzed from both reconstructed slices and a 3D model built by stacking these slices. In the slices data, sand particles exhibit a median size (P50) of $42.1 \mu\text{m}$, while non-sand particles have a smaller median size of $33.1 \mu\text{m}$. This trend holds consistently across the percentiles: for P80, sand particles measure $68.8 \mu\text{m}$ compared to non-sand particles at $55.1 \mu\text{m}$, while at P20, sand particles are $24.3 \mu\text{m}$ versus $18.5 \mu\text{m}$ for non-sand particles. These measurements demonstrate a general pattern where sand particles are consistently larger than non-sand particles. The 3D model data supports these findings, with sand particles having a P50 of $42.8 \mu\text{m}$ and non-sand particles $30.7 \mu\text{m}$. Additionally, both P80 and P20 values further validate this pattern, with sand particles remaining larger than non-sand particles. The P80 value for sand particles,

however, shows a noticeable difference between the slices and 3D model data: $68.8 \mu\text{m}$ in slices and $87.3 \mu\text{m}$ in the 3D model. This discrepancy is likely due to over-segmentation of larger particles when employing the watershed segmentation technique on slice data, a limitation potentially introduced by the method's sensitivity to particle boundaries. Despite this minor variation in the P80 values for sand particles, the results between the slices and 3D model are generally consistent within the constraints of the $6.5 \mu\text{m}$ detector resolution. This consistency indicates that particle size distribution derived from individual slices can provide reliable results, particularly for medium and smaller particle sizes. It

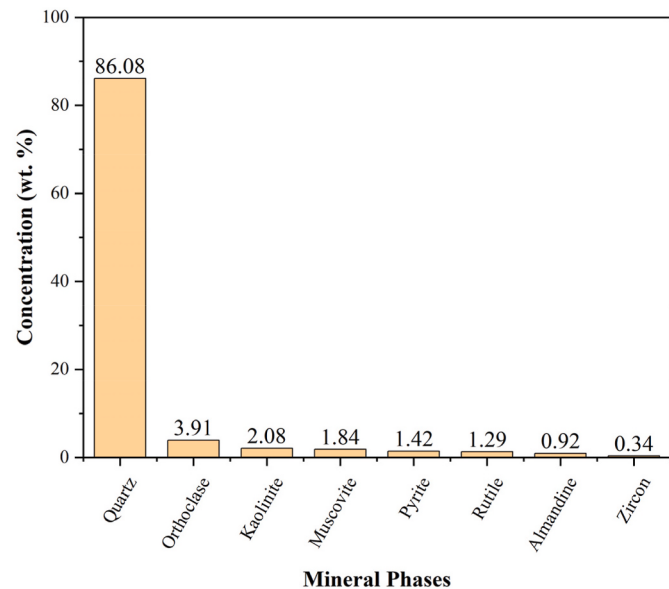


Fig. 9. Mineral phases of solid particles in bitumen froth identified by modal mineralogy.

Table 1

The particle size distribution of sand and non-sand minerals analyzed from the reconstructed slices and their stacked 3D model.

Images	Particle type	Particle size distribution (μm)		
		P80	P50	P20
Slices	Sand	68.8	42.1	24.3
	Non-sand	55.1	33.1	18.5
3D model	Sand	87.3	42.8	19.9
	Non-sand	50.8	30.7	17.4

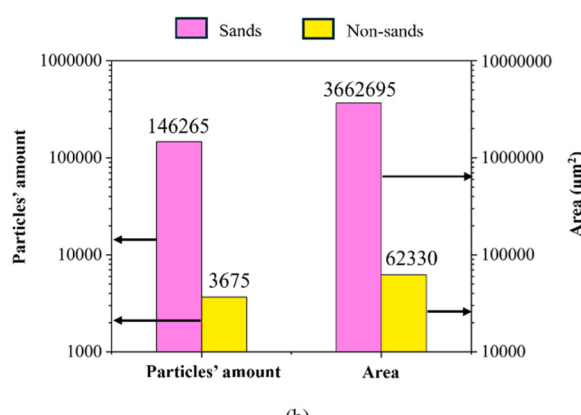
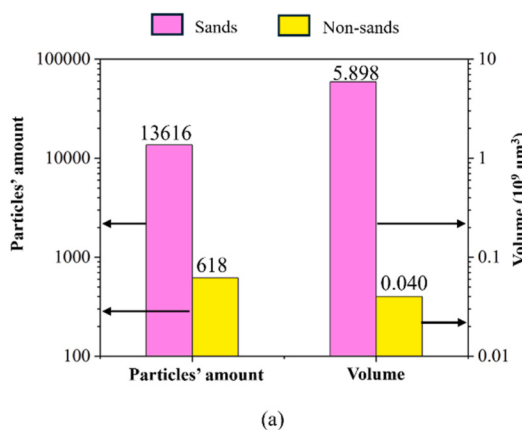


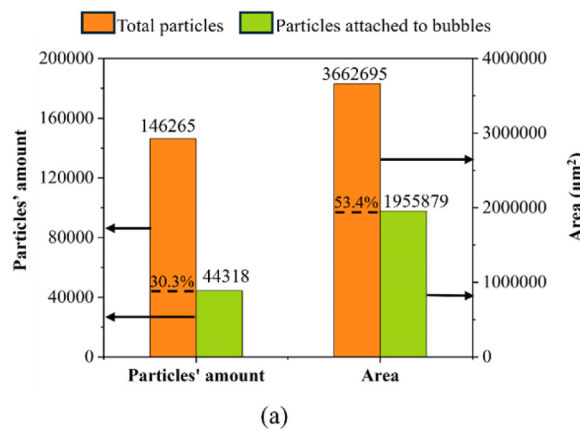
Fig. 8. Amount and occupied volume/area of sand and non-sand particles analyzed from (a) 3D model, and (b) reconstructed slices displayed in semi-logarithmic chart.

reinforces that the slice-based quantification aligns well with 3D model results, establishing slices as a valid approach for preliminary analysis.

These findings highlight the potential effectiveness of using synchrotron-based micro-CT imaging with advanced segmentation techniques in providing accurate, real-time particle size quantification. The synchrotron-based micro-CT imaging not only visualizes the internal structure of bitumen froth with high clarity but also achieves a level of accuracy in particle size distribution analysis that is comparable to conventional off-site methods (Wang et al., 2021; Stasiuk and Schramm, 2001). This capability is particularly valuable for on-site evaluations, offering a precise and reliable alternative to traditional mineral particle analysis methods and ensuring robust data for both research and industrial applications.

3.2. True flotation particles

As mentioned previously, we developed an innovative image transformation technique, successfully identified particles attached to air bubbles as shown in Fig. 6. The particles attached to air bubbles are considered to be brought directly to the froth layer through true flotation in forth flotation process. From the reconstructed slices, we quantified the particle size distribution of particles attaching to bubbles (i.e., those carried over to the froth layer due to true flotation attaching to air bubbles) and those not attaching to air bubbles (i.e., transfer to froth layer by other means, such as slime coating or mechanical entrainment). The amount and covered area of true flotation particles are summarized in Fig. 10. In the analysis of sand particles, 44,318 sand particles out of 146,265 (30.3% of the total sand particles) were found to be true flotation particles, covering an area of 1,955,879 μm^2 (53.4% of the total area occupied by sand particles). True flotation particles make up 30.3% of the total count but occupy more than half of the total area (53.4%). This suggests that the average size of the true flotation particles is larger than that of the free particles that are not attached to bubbles. Additionally, the particles not attached to bubbles, despite being more numerous, covering less area, indicating they were predominantly consisting of smaller particles. Similarly, for the non-sand particles, 434 particles (11.8%) were carried over through true flotation, covering an area of 18,325 μm^2 (29.4% of the total non-sand particle area). That is to say, both sand particles and non-sand particles that are reported into froth layer though true flotation tend to exhibit relatively larger sizes. This result is reasonable because particles in oil sands are generally coated with bitumen, giving them high hydrophobicity (Wang et al., 2022). Hydrophobic particles tend to enter the forth layer through true flotation during the flotation process (George et al., 2004), while particles that are too fine are less likely to interact with bubbles (Wang and Liu, 2021b). Therefore, particles entering bitumen forth through true flotation in oil sands flotation are expected to have larger sizes.



(a)

Additionally, Zhou et al. (2017b) analyzed the flotation behavior of fine solids (<44 μm) extracted from oil sands and found that the recovery of hydrophobic solids by true flotation increases with particle size. In addition, it should be noted that particles of the same type of mineral have the same density, so the proportion of the area occupied by true flotation particles to the total particle area also represents the proportion of the mass of particles attached to bubbles to the total particle mass.

It is very interesting to dig deeper based on the quantitative analysis of particles at two different positions: attaching to or not attaching to air bubbles. The particle size distribution is revealed in Fig. 11. A significant difference between sand particles attaching to air bubbles and those not attached is observed. Specifically, the median particle size (P50) for sand particles attached to air bubbles is 67.6 μm , whereas for those not attached, it is only 35.7 μm . For non-sand particles, the median size (P50) is 35.3 μm for attached particles and 30.6 μm for those not attached, showing less variation compared to sand particles. This observation suggests that for mineral solids entering the froth layer, larger particles predominantly undergo true flotation, attaching directly to air bubbles, while smaller particles are more likely to enter the froth through slime coating or mechanical entrainment. This suggests that particle size plays a critical role in the flotation behavior, which is consistent with observations in mineral flotation (Zhou et al., 2017b). In oil sands flotation, any particles entering the froth layer are undesirable. To minimize the amount of particles in the froth layer, methods such as flocculation can be considered to reduce the content of fine particles. However, larger particles entering the froth layer through true flotation can still result in a significant presence of solids in the bitumen froth. It is therefore essential to adopt measures to suppress these particles, such as

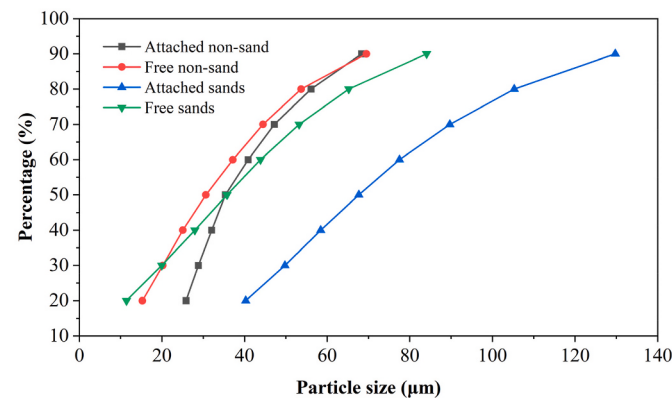
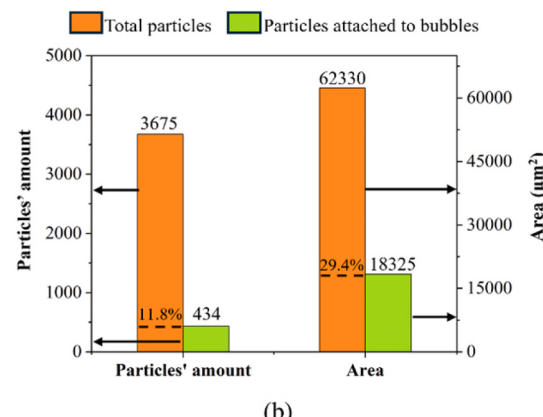


Fig. 11. The particle size distribution for attached non-sand particles, free non-sand particles, attached sand particles, and free sand particles.



(b)

Fig. 10. Amount and covered area of total particles and particles attached to bubbles (i.e., true flotation particles) for (a) sand, and (b) non-sand minerals.

adding suitable depressants or employing agents that promote the effective release of bitumen from the particle surface and reduce their hydrophobicity. Although previous studies have mentioned both true flotation and entrainment as mechanisms for particle transfer into the froth, direct evidence of these phenomena has been limited. In this study, clear quantitative data and visualization that offer direct insight into by which mechanism the unwanted particles transfer into froth layer were provided.

4. Conclusion

Synchrotron-based micro-CT was used to directly visualize the distribution of solids in the fresh bitumen forth. Through the in-situ analysis of over 14,000 particles and the 3D model built from X-ray images, we successfully segmented and quantified both sand and non-sand particles. Sand particles are predominant, making up 98.9% by weight. Non-sand particles, constituting only 1.1% by weight. Consistent results regarding the mineral composition and content of particles within the bitumen froth were achieved through MLA analysis, indicating that this image-based analytical method demonstrates a high degree of accuracy. In addition, the median particle size (P50) for sand particles is 42 µm, with non-sand minerals smaller in size compared to sand particles. These findings are almost identical to the results obtained by traditional off-site (Dean Stark) methods, further confirming the accuracy of this advanced imaging technique.

A major contribution of this study is the successful identification of true flotation particles (both sands and non-and). Particles were differentiated based on their attachment to air bubbles, achieved through our imaging, transformation and segmentation methods. Particles attached to bubbles in bitumen froth were considered to enter the froth specifically through true flotation, while the remaining particles enter the froth layer for other reasons such as entrainment by water or entrapment by bitumen. Notably, approximately 30.3% of sand particles were attached to bubbles, covering over 53% of the area occupied by sand particles, indicating a trend where large particles are more likely to attach to air bubbles and be carried through true flotation. In comparison, smaller particles tend to be transported into the froth layer by mechanisms other than true flotation. Therefore, to minimize the particle content in bitumen froth product during oil sands flotation, it is necessary to simultaneously reduce the fine particle content through measures such as adding flocculants and suppress the entry of coarse particles into the froth layer by true flotation by reduce their hydrophobicity.

This finding underscores the critical role particle size plays in flotation behavior, providing quantitative evidence supporting hypotheses on flotation and entrainment mechanisms. The insights gained from this study hold significant implications for optimizing oil sands processing. By enabling real-time, high-resolution observation of particle size distribution and transport mechanisms, synchrotron-based imaging provides a powerful tool for on-site evaluations, offering a reliable alternative to off-site methods. Future research could focus on further refining this approach by integrating higher-resolution detectors to capture finer details of mineral particles, particularly for heavy minerals below the current resolution threshold. Additionally, addressing slime coating and its impact on particle behavior in bitumen froth could enhance understanding of unwanted fine particle carryover, providing a pathway to improved separation efficiency in oil sands processing.

CRediT authorship contribution statement

Hanyu Zhang: Writing – review & editing, Writing – original draft, Investigation, Formal analysis. **Liuyin Xia:** Writing – review & editing, Supervision, Resources, Project administration, Methodology, Investigation, Funding acquisition, Formal analysis, Conceptualization. **Ning Zhu:** Resources, Methodology, Data curation. **Sergey Gasilov:** Resources, Methodology, Data curation. **Iris He:** Formal analysis, Data

curation. **Xiaofan Ding:** Formal analysis, Data curation.

Declaration of generative AI and AI-assisted technologies in the writing process

During the preparation of this work the authors used ChatGPT 40 in order to check the grammar. After using this tool, the authors reviewed and edited the content as needed and take full responsibility for the content of the publication.

Declaration of competing interest

The authors declare that they have no known competing financial interests or personal relationships that could have appeared to influence the work reported in this paper.

Acknowledgements

This work was supported by Imperial Oil Resources Limited and Alberta Innovates through the Institute for Oil Sands Innovation at the University of Alberta (IOSI) and the start-up funding from the Faculty of Engineering at the University of Alberta. The research described in this paper was partially performed at the Canadian Light Source (CLS), a national research facility of the University of Saskatchewan, which is supported by the Canada Foundation for Innovation (CFI), the Natural Sciences and Engineering Research Council (NSERC), the National Research Council (NRC), the Canadian Institutes of Health Research (CIHR), the Government of Saskatchewan, and the University of Saskatchewan. The authors are also grateful for the assistance from Dr. Qi Liu and Dr. Natalia Semagina of the Department of Chemical and Materials Engineering at the University of Alberta.

Data availability

Data will be made available on request.

References

- Adams, F., Janssens, K., Snigirev, A., 1998. Microscopic X-ray fluorescence analysis and related methods with laboratory and synchrotron radiation sources. *Journal of Analytical Atomic Spectrometry* 13 (5), 319–331. <https://doi.org/10.1039/A707100K>.
- Anzoom, S.J., Bourinval, G., Ata, S., 2024. Micro-CT imaging of a frozen bubble cluster: sample holder development and image processing techniques. *Separation and Purification Technology* 335, 126111. <https://doi.org/10.1016/j.seppur.2023.126111>.
- Bravin, A., Coan, P., Suortti, P., 2012. X-ray phase-contrast imaging: from pre-clinical applications towards clinics. *Phys. Med. Biol.* 58 (1), R1. <https://doi.org/10.1088/0031-9155/58/1/R1>.
- Chen, X., Verma, R., Espinoza, D.N., Prodanović, M., 2018. Pore-scale determination of gas relative permeability in hydrate-bearing sediments using X-ray computed microtomography and lattice Boltzmann method. *Water Resour. Res.* 54 (1), 600–608. <https://doi.org/10.1002/2017WR021851>.
- Dracos, T., 1996. Particle tracking velocimetry (PTV) basic concepts. In: *Three-Dimensional Velocity and Vorticity Measuring and Image Analysis Techniques: Lecture Notes from the Short Course Held in Zürich, Switzerland*. Springer, Dordrecht, pp. 155–160.
- Estevadeordal, J., Goss, L., 2005. PIV with LED: particle shadow velocimetry (PSV) technique. In: *43rd AIAA Aerospace Sciences Meeting and Exhibit*, p. 37.
- Faraogó, T., Gasilov, S., Emslie, I., Zuber, M., Helfen, L., Vogelgesang, M., Baumbach, T., 2022. Tofu: a fast, versatile and user-friendly image processing toolkit for computed tomography. *J. Synchrotron Radiat.* 29 (3), 916–927. <https://doi.org/10.1107/S160057752200282X>.
- García-Moreno, F., Kamn, P.H., Neu, T., Heim, K., Rack, A., Banhart, J., 2017. In situ X-ray tomography of aqueous foams: analysis of columnar foam generation. *Colloids Surf. A Physicochem. Eng. Asp.* 534, 78–84. <https://doi.org/10.1016/j.colsurfa.2017.03.011>.
- George, P., Nguyen, A.V., Jameson, G.J., 2004. Assessment of true flotation and entrainment in the flotation of submicron particles by fine bubbles. *Miner. Eng.* 17 (7–8), 847–853. <https://doi.org/10.1016/j.mineng.2004.02.002>.
- Ghorbani, Y., Becker, M., Petersen, J., Morar, S.H., Mainza, A., Franzidis, J.P., 2011. Use of X-ray computed tomography to investigate crack distribution and mineral dissemination in sphalerite ore particles. *Miner. Eng.* 24 (12), 1249–1257. <https://doi.org/10.1016/j.mineng.2011.04.008>.

- Heitkam, S., Rudolph, M., Lappan, T., Sarma, M., Eckert, S., Trtik, P., Lehmann, E., Vontobel, P., Eckert, K., 2018. Neutron imaging of froth structure and particle motion. Miner. Eng. 119, 126–129. <https://doi.org/10.1016/j.mineng.2018.01.021>.
- Hooshiar, A., Uhlik, P., Ivey, D.G., Liu, Q., Etzell, T.H., 2012. Clay minerals in nonaqueous extraction of bitumen from Alberta oil sands: Part 2. Characterization of clay minerals. Fuel Process. Technol. 96, 183–194. <https://doi.org/10.1016/j.fuproc.2011.10.010>.
- Kaminsky, H.A., 2008. Characterization of an Athabasca oil sand ore and process streams. <https://doi.org/10.7939/r3-60y0-hk65>.
- Kamm, P.H., García-Moreno, F., Neu, T.R., Heim, K., Mokso, R., Banhart, J., 2017. Fast synchrotron X-ray tomography of dynamic processes in liquid aluminium alloy foam. Adv. Eng. Mater. 19 (11), 1600550. <https://doi.org/10.1002/adem.201600550>.
- Khattak, M.A., Yasin, N.S., Andjani, H.N., Tajuddin, P.N., Narajah, S., Fei, S.Z., et al., 2018. Global energy security and North America: a review. Journal of Advanced Research in Applied Sciences and Engineering Technology 11 (1), 82–98.
- Khodaei, Booran S., Wang, X., Tan, X., Liu, Q., 2020. Effect of carbon dioxide on asphaltene precipitation from bitumen–heptane mixtures. Energy & Fuels 34 (8), 9483–9491. <https://doi.org/10.1021/acs.energyfuels.0c01562>.
- Kohler, R., 1981. A segmentation system based on thresholding. Comput. Graph. Image Process. 15 (4), 319–338. [https://doi.org/10.1016/S0146-664X\(81\)80015-9](https://doi.org/10.1016/S0146-664X(81)80015-9).
- Kotlyar, L.S., Sparks, B.D., Woods, J.R., Raymond, S., Le Page, Y., Shelfantook, W., 1998. Distribution and types of solids associated with bitumen. Petrol. Sci. Technol. 16 (1–2), 1–9. <https://doi.org/10.1080/10916469808949769>.
- L'Annunziata, Michael F., 2023. Electromagnetic radiation: photons. In: Radioactivity, third ed. Elsevier, pp. 709–746. <https://doi.org/10.1016/B978-0-323-90440-7.00005-3>.
- Lappan, T., Sarma, M., Heitkam, S., Trtik, P., Mannes, D., Eckert, K., Eckert, S., 2020. Neutron radiography of particle-laden liquid metal flow driven by an electromagnetic induction pump. Magnetohydrodynamics 56 (2/3), 167–176. <https://doi.org/10.22364/mhd.56.2-3>.
- Lappan, T., Herting, D., Ziauddin, M., Stenzel, J., Shevchenko, N., Eckert, S., Eckert, K., Heitkam, S., 2023. X-Ray particle tracking velocimetry in an overflowing foam. Appl. Sci. 13 (3), 1765. <https://doi.org/10.3390/app13031765>.
- Li, A., Xu, Z., 2020. Determination of clay content in Canadian oil sands using x-ray fluorescence spectroscopy for diagnosis of ore processability. Can. J. Chem. Eng. 98 (1), 360–372. <https://doi.org/10.1002/cjce.23599>.
- Lifton, J.J., Malcolm, A.A., 2021. Estimating the product of the X-ray spectrum and quantum detection efficiency of a CT system and its application to beam hardening correction. Sensors 21 (9), 3284. <https://doi.org/10.3390/s21093284>.
- Liu, Q., Cui, Z., Etzell, T.H., 2006. Characterization of Athabasca oil sands froth treatment tailings for heavy mineral recovery. Fuel 85 (5–6), 807–814. <https://doi.org/10.1016/j.fuel.2005.08.032>.
- Marr, D., Hildreth, E., 1980. Theory of edge detection. Proceedings of the Royal Society of London. Series B. Biological Sciences 207 (1167), 187–217. <https://doi.org/10.1098/rspb.1980.0020>.
- Masliyah, J., Zhou, Z.J., Xu, Z., Czarnecki, J., Hamza, H., 2004. Understanding water-based bitumen extraction from Athabasca oil sands. Can. J. Chem. Eng. 82 (4), 628–654. <https://doi.org/10.1002/cjce.5450820403>.
- Mathews, J.P., Campbell, Q.P., Xu, H., Halleck, P., 2017. A review of the application of X-ray computed tomography to the study of coal. Fuel 209, 10–24. <https://doi.org/10.1016/j.fuel.2017.07.079>.
- McCosh, R., 1996. Geology executive summary from mineral development agreement. Final report, Alberta chamber of resources.
- Mhonde, N.P., Wiese, J.G., McFadzean, B., 2017. Comparison of collector performance for a South African and a Brazilian iron ore considering mineralogical characteristics. Miner. Eng. 113, 55–67. <https://doi.org/10.1016/j.mineng.2017.08.006>.
- Miller, J.D., Lin, C.L., Hupka, L., Al-Wakeel, M.I., 2009. Liberation-limited grade/recovery curves from X-ray micro CT analysis of feed material for the evaluation of separation efficiency. Int. J. Miner. Process. 93 (1), 48–53. <https://doi.org/10.1016/j.minpro.2009.05.009>.
- Polschuk, C., Elieza, J., Vedachalam, S., Dalai, A.K., Adjaye, J., 2023. A review of foulant sources, operational issues, and remedies during the processing of oil sand derived bitumen fractions. Fuel 340, 127516. <https://doi.org/10.1016/j.fuel.2023.127516>.
- Rack, A., Garcia-Moreno, F., Schmitt, C., Betz, O., Cecilia, A., Ershov, A., Rack, T., Banhart, J., Zabler, S., 2010. On the possibilities of hard X-ray imaging with high spatio-temporal resolution using polychromatic synchrotron radiation. J. X Ray Sci. Technol. 18 (4), 429–441. <https://doi.org/10.3233/XST-2010-0273>.
- Raffel, M., Willert, C.E., Scarano, F., Kähler, C.J., Wereley, S.T., Kompenhans, J., 2018. Particle Image Velocimetry: a Practical Guide. Springer.
- Rana, R., Nanda, S., Dalai, A.K., Kozinski, J.A., Adjaye, J., 2019. Synthetic crude processing: impacts of fine particles on hydrotreating of bitumen-derived gas oil. In: Fuel Processing and Energy Utilization, vol. 22. Chapman and Hall/CRC, pp. 187–206.
- Rao, F., Liu, Q., 2013. Froth treatment in Athabasca oil sands bitumen recovery process: a review. Energy & fuels 27 (12), 7199–7207. <https://doi.org/10.1021/ef4016697>.
- Record high crude oil production largely driven by oil sands: Crude oil production year in review 2023. Available at: <https://www.statcan.gc.ca/ol/en/plus/5781-record-high-crude-oil-production-largely-driven-oil-sands-crude-oil-year-review-2023>.
- Ross, V.E., 1997. Particle-bubble attachment in flotation froths. Miner. Eng. 10 (7), 695–706. [https://doi.org/10.1016/S0892-6875\(97\)00049-6](https://doi.org/10.1016/S0892-6875(97)00049-6).
- Seal, A., Das, A., Sen, P., 2015. Watershed: an image segmentation approach. Int. J. Comput. Sci. Inf. Technol. 6 (3), 2295–2297.
- Siwek, B., Zembala, M., Pomianowski, A., 1981. A method for determination of fine-particle floatability. Int. J. Miner. Process. 8 (1), 85–88. [https://doi.org/10.1016/0301-7516\(81\)90009-0](https://doi.org/10.1016/0301-7516(81)90009-0).
- Solórzano, E., Pardo-Alonso, S., De Saja, J.A., Rodríguez-Pérez, M.A., 2013. Study of aqueous foams evolution by means of X-ray radioscoppy. Colloids Surf. A Physicochem. Eng. Asp. 438, 159–166. <https://doi.org/10.1016/j.colsurfa.2013.01.052>.
- Stasiuk, E.N., Schramm, L.L., 2001. The influence of solvent and demulsifier additions on nascent froth formation during flotation recovery of Bitumen from Athabasca oil sands. Fuel Process. Technol. 73 (2), 95–110. [https://doi.org/10.1016/S0378-3820\(01\)00197-7](https://doi.org/10.1016/S0378-3820(01)00197-7).
- Trahar, W.J., 1981. A rational interpretation of the role of particle size in flotation. Int. J. Miner. Process. 8 (4), 289–327. [https://doi.org/10.1016/0301-7516\(81\)90019-3](https://doi.org/10.1016/0301-7516(81)90019-3).
- Tropea, C., Yarin, A.L., Foss, J.F. (Eds.), 2007. Springer Handbook of Experimental Fluid Mechanics. Springer, Berlin.
- Wang, D., Liu, Q., 2021a. Influence of aggregation/dispersion state of hydrophilic particles on their entrainment in fine mineral particle flotation. Miner. Eng. 166, 106835. <https://doi.org/10.1016/j.mineng.2021.106835>.
- Wang, D., Liu, Q., 2021b. Hydrodynamics of froth flotation and its effects on fine and ultrafine mineral particle flotation: a literature review. Miner. Eng. 173, 107220. <https://doi.org/10.1016/j.mineng.2021.107220>.
- Wang, L., Peng, Y., Runge, K., Bradshaw, D., 2015. A review of entrainment: mechanisms, contributing factors and modelling in flotation. Miner. Eng. 70, 77–91. <https://doi.org/10.1016/j.mineng.2014.09.003>.
- Wang, D., Qiao, C., Zhao, Z., Yang, W., Chen, H., Yin, T., Yan, Z., Wu, M., Mao, X., Santander, C., Liu, Q., 2021. Understanding the properties of bitumen froth from oil sands surface mining and treatment of water-in-oil emulsions. Energy & Fuels 35 (24), 20079–20091. <https://doi.org/10.1021/acs.energyfuels.1c03370>.
- Wang, D., Tao, H., Wang, D., Wang, K., Tan, X., Liu, Q., 2022. Effects of mineral surface silanization and bitumen coating on its filtration from an aqueous slurry. Fuel 325, 124921. <https://doi.org/10.1016/j.fuel.2022.124921>.
- Warren, L.J., 1985. Determination of the contributions of true flotation and entrainment in batch flotation tests. Int. J. Miner. Process. 14 (1), 33–44. [https://doi.org/10.1016/0301-7516\(85\)90012-2](https://doi.org/10.1016/0301-7516(85)90012-2).
- Waters, K.E., Rowson, N.A., Fan, X., Parker, D.J., Cilliers, J.J., 2008. Positron emission particle tracking as a method to map the movement of particles in the pulp and froth phases. Miner. Eng. 21 (12–14), 877–882. <https://doi.org/10.1016/j.mineng.2008.02.007>.
- Wei, Z., Wiebe, S., Chapman, D., 2013. Ring artifacts removal from synchrotron CT image slices. J. Instrum. 8 (6), C06006. <https://doi.org/10.1088/1748-0221/8/06/C06006>.
- What is a synchrotron? 2024. Canadian Light Source. Available at: <https://www.lightsource.ca/public/what-is-a-synchrotron.php#AboutSynchrotronLight>.
- Wysokinski TW, Chapman D, Adams G, Renier M, Suortti P, Thominson W. Beamlines of the biomedical imaging and therapy facility at the Canadian Light Source-Part 2. InJournal of Physics: Conference Series 2013 Mar 22 (Vol. 425, No. 7, p. 072013). IOP Publishing.25. Fitzgerald, R., Phase-sensitive x-ray imaging. Physics today, 2000. 53 (7): p. 23–26. <https://doi.org/10.1088/1742-6596/425/7/072013>.
- Yu, Y., Ma, L., Cao, M., Liu, Q., 2017. Slime coatings in froth flotation: a review. Miner. Eng. 114, 26–36. <https://doi.org/10.1016/j.mineng.2017.09.002>.
- Zhao, J., Liu, Q., Gray, M.R., 2016. Characterization of fine solids in Athabasca bitumen froth before and after hydrothermal treatment. Energy & Fuels 30 (3), 1965–1971. <https://doi.org/10.1021/acs.energyfuels.5b02325>.
- Zhou, Z.A., Li, H., Chow, R., Adeyinka, O.B., Xu, Z., Masliyah, J., 2017a. Impact of fine solids on mined athabasca oil sands extraction II: Effect of fine solids with different surface wettability on bitumen recovery. Can. J. Chem. Eng. 95 (1), 120–126. <https://doi.org/10.1002/cjce.22564>.
- Zhou, Z.A., Li, H., Chow, R., Adeyinka, O.B., Xu, Z., Masliyah, J., 2017b. Impact of fine solids on mined Athabasca oil sands extraction I: Floatability of fine solids. Can. J. Chem. Eng. 95 (1), 111–119. <https://doi.org/10.1002/cjce.22557>.
- Zhou, J., Li, H., Zhao, L., Chow, R., 2018. Role of mineral flotation technology in improving bitumen extraction from mined Athabasca oil sands: I. Flotation chemistry of water-based oil sand extraction. Can. J. Chem. Eng. 96 (9), 1986–1999. <https://doi.org/10.1002/cjce.23139>.